Last phase of the Little Ice Age forced by volcanic eruptions

Stefan Brönnimann[1,2], Jörg Franke[1,2], Samuel U. Nussbaumer[3], Heinz J. Zumbühl[1,2], Daniel Steiner[4], Mathias Trachsel[1,2,5,6], Gabriele C. Hegerl[7], Andrew Schurer[7], Matthias Worni[1,2], Abdul Malik[1,2,8], Julian Flückiger[1,2], Christoph C. Raible[1,9]

[1] Oeschger Centre for Climate Change Research, University of Bern, Switzerland

[2] Institute of Geography, University of Bern, Switzerland

[3] Department of Geography, University of Zurich Switzerland & Department of Geosciences, University of Fribourg, Switzerland

[4] University of Teacher Education, Bern, Switzerland

[5] Department of Geology, University of Maryland, United States

[6] currently at Department of Geography, University of Wisconsin-Madison, USA

[7] School of Geosciences, University of Edinburgh, UK

[8] currently at Imperial College, London, UK

[9] Climate and Environmental Physics, Physics Institute, University of Bern, Switzerland

During the first half of the 19th century, several large tropical volcanic eruptions occurred within less than three decades. Global climate effects of the 1815 Tambora eruption have been investigated, but those of an eruption in 1808 whose source is unknown and the eruptions in the 1820s and 1830s have received less attention. Here, we analyse the effect of the sequence of eruptions in observations, global three-dimensional climate field reconstructions, and coupled climate model simulations. All eruptions were followed by substantial drops of summer temperature over the Northern Hemisphere land areas. In addition to the direct radiative effect, which lasts 2-3 years, the simulated ocean-atmosphere heat exchange sustained cooling for several years following these eruptions, affecting the slow components of the climate system. Africa was hit by two decades of drought, global monsoons weakened, and the tracks of low-pressure systems over the North Atlantic moved south. The low temperatures and increased precipitation in Europe triggered the last phase of advance of Alpine glaciers. Only after the 1850s the transition into the period of anthropogenic warming started. We conclude that the end of the Little Ice Age was marked by the recovery from a sequence of volcanic eruptions, which makes it difficult to define a single pre-industrial baseline.

The period between around 1350 or 1450 and 1850 is often termed the "Little Ice Age" (LIA). In several regions the LIA was accompanied by glacier advances[1,2]. It might have been initiated by volcanic eruptions[3], but the relative contributions of solar and volcanic forcing remain unclear. Given the regional differences[4] and uncertainties in the mechanism involved, the onset of the LIA is still highly debated[5].

Importantly, the transition from the LIA into the period of anthropogenic warming is also not well understood. After a rather warm phase around 1800, global climate cooled again in the

early 19th century[6] for several decades, accompanied by pronounced glacier advances in the Alps. Recent work therefore dated the start of anthropogenic warming back to the early 19th century[7]. However, the fact that several major tropical volcanoes erupted between 1808 and 1835 (note that there is still large uncertainty – the 1808/09 eruption remains unknown[8] and the attribution of the 1831 eruption has recently been questioned[9]), including the well-studied 1815 Tambora eruption, makes the separation between volcanic and anthropogenic contributions difficult. Based on attribution results, a small drop in greenhouse gas levels during the LIA, and the subsequent recovery and initialization of the industrial era affected Northern Hemisphere (NH) temperatures[10,11]. Peak cold conditions in the early 19th century were dominated by volcanism[11]. However, except for Tambora[12], these eruptions are not well studied, and their contribution to global early 19th century climate is unclear.

In this paper we use an ensemble of global climate field reconstructions based on data assimilation[13] (in the following termed palaeo-reanalysis;see Methods) and analyse it together with instrumental data,[14] existing reconstructions[6,15,16] and climate simulations (HadCM3 and FUPSOL, see Methods)[10,17]. We then study the effects of the volcanic eruptions on different parts of the climate system, including precipitation in the monsoon regions[16] and Alpine glaciers.[18,19]

Cold Northern Extratropical Summers

The coldest ten warm seasons (Apr.-Sep.) over the northern extratropical land areas in the period 1750-1900 in the ensemble mean of the palaeo-reanalysis were exclusively post-eruption seasons (see Methods; Fig. 1a). Those following the early 19th century eruptions were on average 0.5 °C cooler than the 30-yr period preceding the eruption (1779-1808). Instrumental series (except for one all are from Europe) confirm the post-eruption cooling

(Fig. 1a), while their long-term trend might be affected by warm bias due to measurement practices in the early decades[20]. The Crowley et al. temperature reconstruction[6] also shows a predominance of post-volcanic years among the coldest warm seasons (six among the coldest twelve and twelve among the coldest 30 warm seasons) and tracks the palaeo-reanalysis very well. A recovery only occurred around 1850. This is consistent with sustained global cooling after eruptions in volcanic-only simulations[11] and with new global temperature reconstructions.[21]

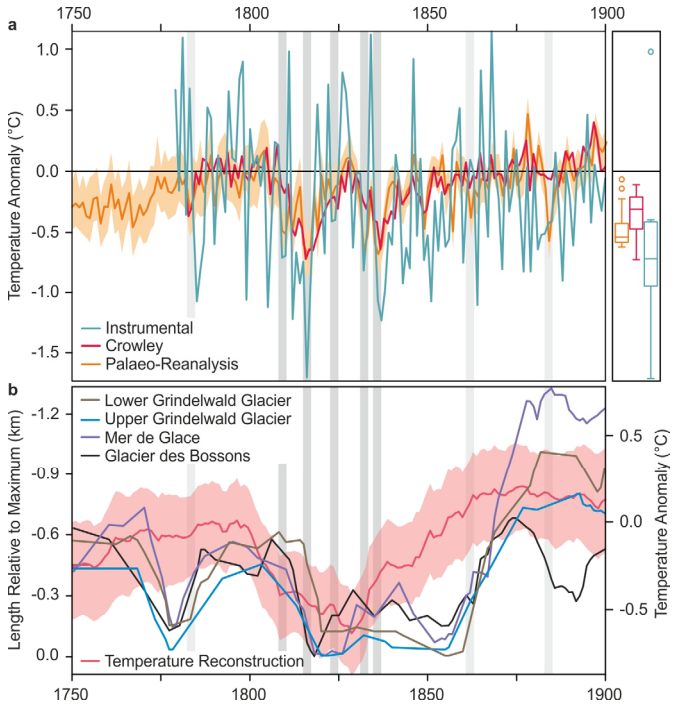

Figure 1 | Climate series for the last part of the Little Ice Age. a Temperature anomalies (with respect to 1779-1808) of northern extratropical land areas (20–90° N) in April-September from the palaeo-reanalysis (orange, ensemble mean; shading denotes the 95% ensemble spread) as well as a reconstruction (30-90° N)[6] (dark red) and the average of 23 early instrumental series (green, see Methods). **b** Length of four well-documented Alpine glaciers[38-40] relative to the minimum in the displayed period as well as 30-yr running means of Alpine summer temperature from a multiproxy reconstruction[15] (red, shading denotes the 95% confidence interval, see Methods; the curve is advanced by 5yrs, approximating the glacier response). Bars indicate volcanic eruptions. Box plots with quartiles and interquartile range in **a** show the post-volcanic seasons of the five early 19th century eruptions.

Anomaly fields for temperature in the palaeo-reanalysis (Fig. 2), which is well constrained by instrumental, documentary and tree ring data (indicated by dashed and solid lines) over northern extratropical land areas, but little elsewhere, exhibit the expected pattern of radiatively forced change. This includes large-scale cooling over the extratropical land masses in the 3 years following volcanic eruptions.

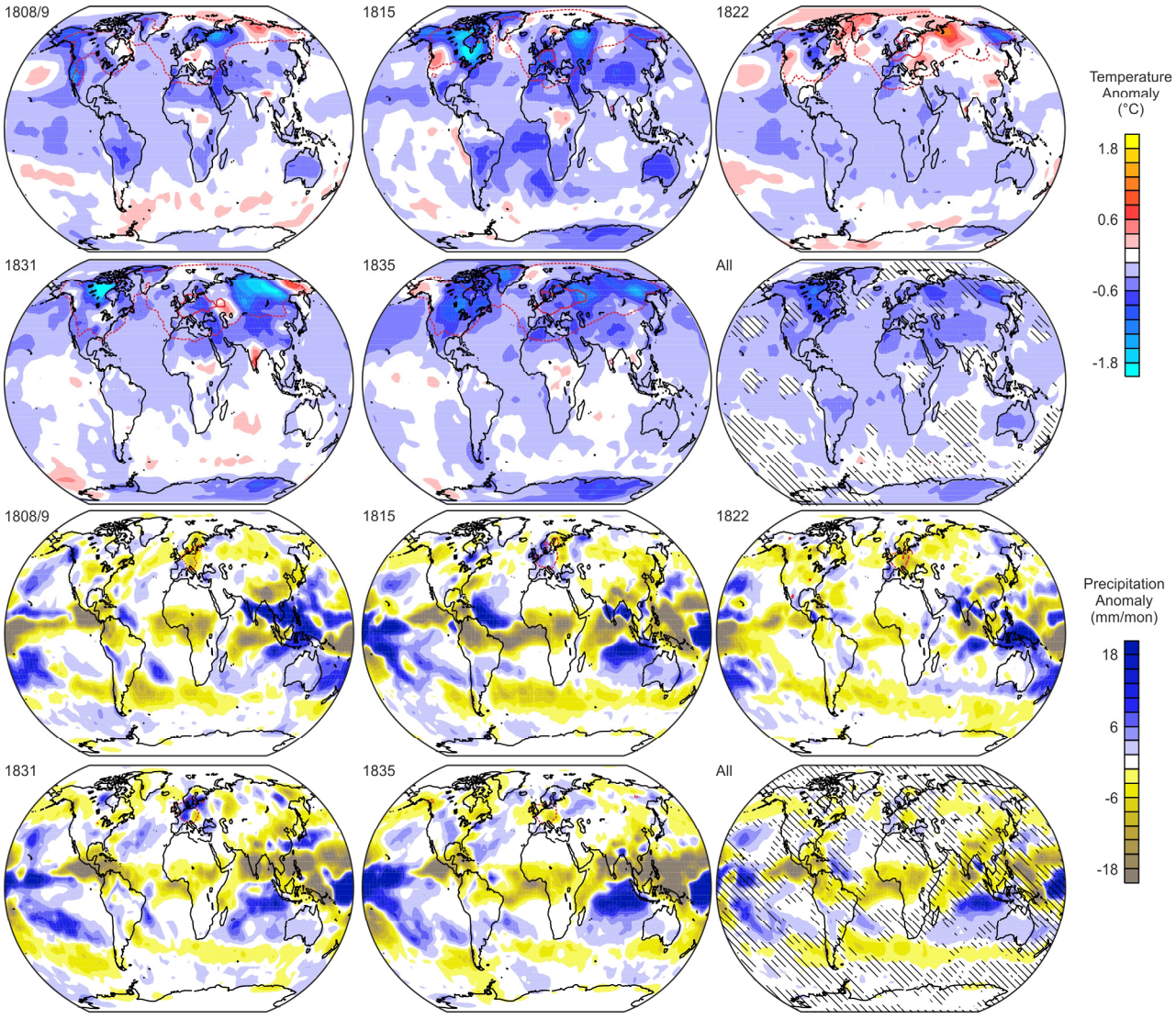

Figure 2 | Post-volcanic anomalies in April-September in the palaeo-reanalysis (ensemble mean). Top: Temperature, bottom: Precipitation. Anomalies are relative to 1779-1808. Solid and dashed lines indicate areas where the reduction of the ensemble spread due to the assimilation reaches 75% and 25%, respectively. Eruptions (analysed seasons) are: unknown Dec. 1808 (1809-1811), Tambora Apr. 1815 (1815-1817), Galanggung Oct. 1822 (1823-1824), unknown (Babuyan Claro?) Sep. 1831 (1832-1833), Cosigüina Jan. 1835

(1835-1837). Panels "All" show the average over all five eruptions, hatching indicates where the sign agrees for less than four.

Reconstructions of climatic variables also show substantial changes on a decadal scale during these years, as is shown in Fig. 1b for a multiproxy reconstruction of summer temperature for the Alps.[15] Even for 30-year averages, a temperature change of 0.65 °C is found between the late 18th and early 19th century, likely related to the coincidence of five strong tropical eruptions (Fig. 1b). This change is highly significant and highlights the difficulty of defining a single pre-industrial reference climate[22,23].

Weak Monsoons

With regard to precipitation anomalies after eruptions, the palaeo-reanalysis (Figs. 2 and 3a) shows decreased rainfall in the African monsoon region immediately following each eruption. This result mainly arises from the model response to the forcing as precipitation is only weakly constrained in the palaeo-reanalysis; it is also found in model studies.[24] Completely independent reconstructions of African dryness back to 1800 based on documentary data (such as lake levels or Nile river flow), though partly infilled, confirm that all post-eruption years (except after the Galanggung eruption 1822) were dry in the African monsoon region[16] (Fig. 3a). According to both data sets the region remained dry during most of the first half of the 19th century.

We further analysed other monsoon regions and compared the palaeo-reanalysis with independent observations[25,26]. We find a weakening of all India monsoon rainfall (Fig. 3b) and of the strength of the Australian monsoon lasting deveral decades (Fig. 3c; the offset between the curves is due to different standardisation periods) in observations. The palaeo-reanalysis, which is largely unconstrained with respect to monsoon precipitation, shows

similar multidecadal variability (though no clear post-volcanic signal). Weak monsoons continued through the 1840s and early 1850s. Can such a long-lasting effect be explained climatically?

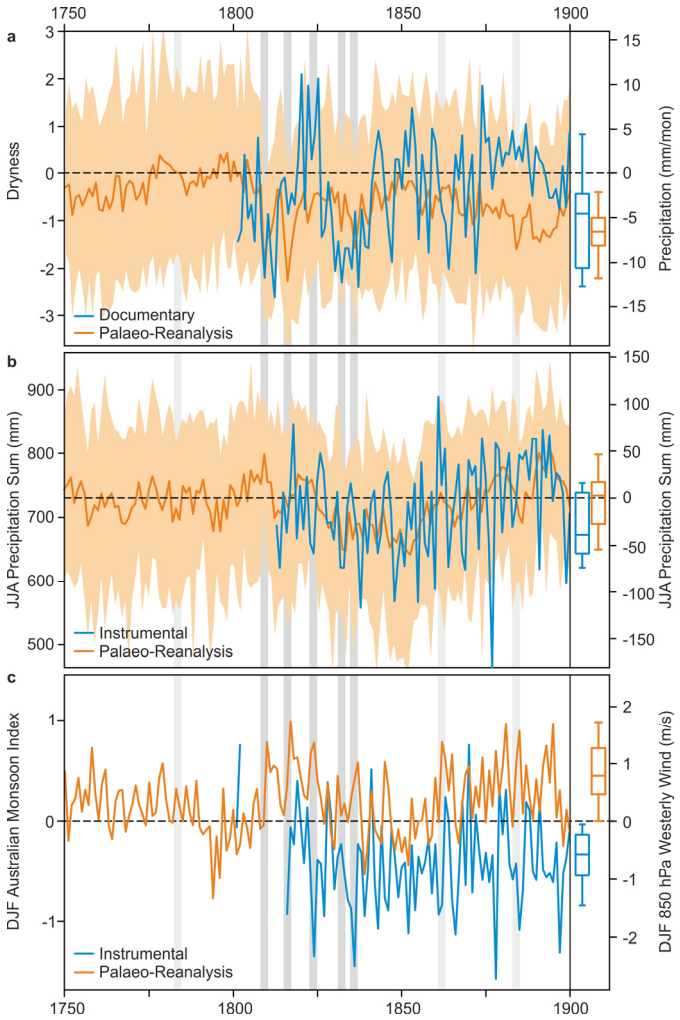

Figure 3 | Change in global monsoon systems. a Dryness index for the African monsoon region [0-20° N, 20° W-30° E] from documentary data[16] (blue) and precipitation (Apr.-Sep.) in the palaeo-reanalysis in the same area (orange). **b** All India Monsoon Rainfall (Jun.-Aug.) in observations[25] (blue) and in the palaeo-reanalysis [67-98° E, 5-36° N] (orange), **c** Australian monsoon index (Dec.-Feb.) in observations[26] (blue, number of days with westerly winds at the surface in the region [98-138° E, 18-5° S], standardized relative to 1800-2014) and of 850 hPa westerly wind in the palaeo-reanalysis in the same region (orange). Observations are on the left scale, palaeo-reanalysis data (right scales, lines are ensemble means, shading denotes the 95% ensemble spread; not

shown in **c** as it fills the panel) are anomalies from 1779-1808. Bars indicate volcanic eruptions. Box plots show the post-volcanic seasons of the five early 19th century eruptions.

Ocean memory integrates weather and climate noise[27], and precipitation anomalies in the African monsoon region may trigger decadal dryness by means of land-surface feedback processes.[28] Therefore, a sequence of eruptions leading to cooling in Europe and land areas globally, as well as drying in Africa and in monsoon regions globally may lead to persisting effects in the climate system. Thus, we analysed two ensembles of coupled simulations (FUPSOL and HadCM3) to identify persisting climate signals in the oceans. Global annual mean surface air temperatures (Fig. 4c) cool by 0.15-1 °C in the two years following each eruption (note that the 1822 Galanggung eruption was not in the model forcing of either model, and the 1861 Dubbi eruption only in HadCM3). The differences between the two ensembles reflect different volcanic forcing (as evidenced in top-of-atmosphere net shortwave radiation; Fig. 4a) and arguably different sensitivities. In both ensembles, annual mean temperatures of the 1770s to 1800s were only reached again in the 1840s and 1850s.[10]

Oceanic response

To address mechanisms for possible sustained effects of this sequence of eruptions, we analysed surface energy fluxes (Fig. 4b) and upper ocean heat content (Fig. 4d). In response to the decreased short-wave forcing, the upper-ocean cools. In a simple mixed-layer-deep ocean model,[29] the effect of a volcanic eruption on the mixed layer is expected to decay within about 2-3 years, but mixing into the deep ocean can lead to delayed ('recalcitrant') responses that accumulate between eruptions.[30] In our simulations, the global upper ocean (0-700 m) heat content is substantially reduced after each eruption, consistent with other simulations[31,32] (the differences between FUPSOL and HadCM3 indicate possible drifts

caused by different volcanic histories affecting the centennial time scale[33]). Upper-ocean heat content does not recover to the 1779-1808 value until the 1860s (in FUPSOL) or even the 1930s (in HadCM3). This is consistent with a possible temporary slow-down in sea-level rise in the 19th century found in some reconstructions.[34]

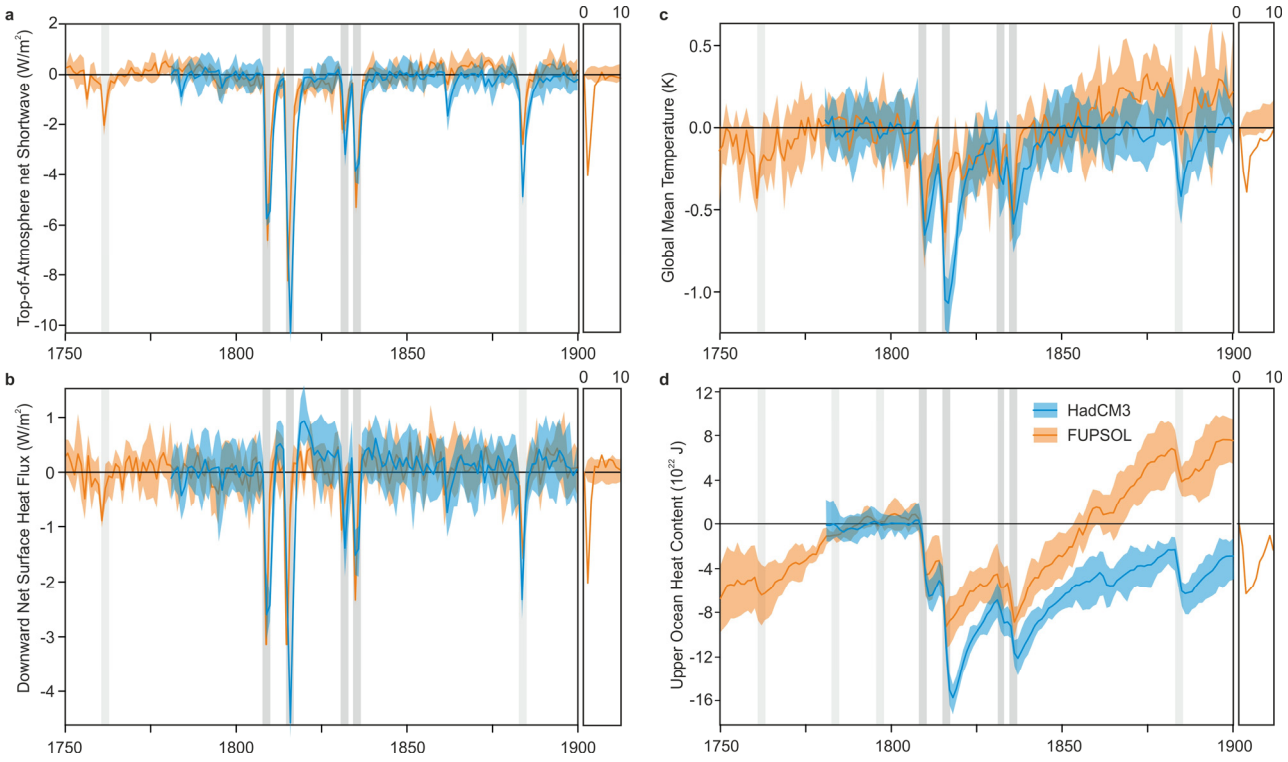

Figure 4 | Global annual means of energy fluxes, temperature and ocean heat content in coupled model simulations (ensemble mean and range). Shown are (**a**) the top of atmosphere net shortwave flux, (**b**) the downward net surface heat flux, (**c**) global mean surface air temperature and (**d**) global upper ocean heat content (0-700 m). Anomalies are relative to 1780-1808, shading indicates the ensemble range, bars indicate volcanic eruptions. Insets indicate composites over all eruptions in the FUPSOL simulations (1600-2000) for the first 10 years, referenced to the year before the eruption (see Methods), with shadings indicating 95% confidence intervals from Monte Carlo simulations.

This is related to changes in oceanic heat uptake. The net surface heat flux (net surface short and longwave radiation minus upward sensible and latent heat fluxes, Fig. 4b) reaches highest upward anomalies (less energy input into the oceans, negative spikes in Fig. 4b) immediately

after the eruptions. The opposite is the case after ca. 3 years, when the short-wave forcing ceases. During this recovery phase, oceans take up heat and recharge their heat content, leading to slight but sustained positive anomalies compared to the years prior to the eruptions. This effect is particularly clear in HadCM3, where ca. 3 years after the 1808/9 and the Tambora eruptions all 10 members exhibit anomalously positive downward heat flux for several years (Fig. 4b). This effect also appears as statistically significant in FUPSOL when composited over all simulated eruptions (right insets) and it was found in several other studies.[31,32]

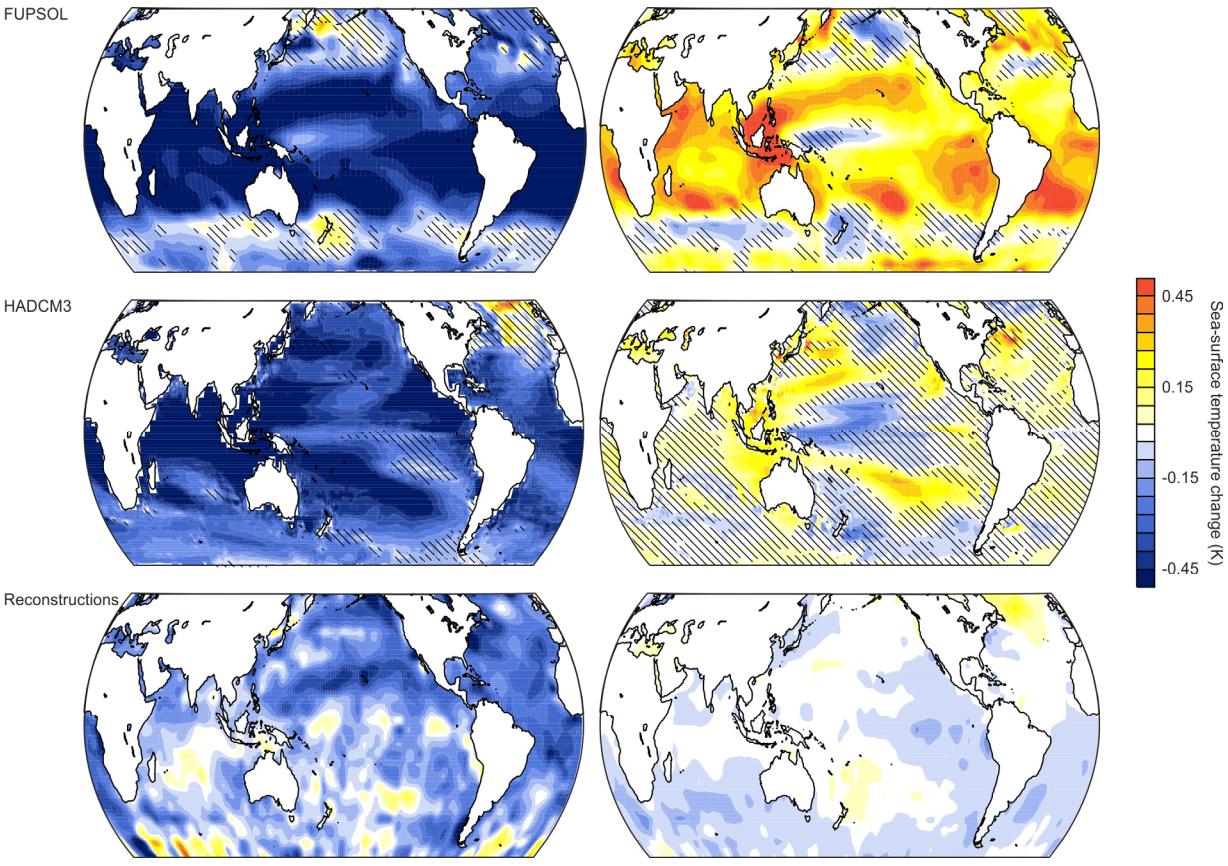

Figure 5 | Annual mean sea-surface temperature changes in HadCM3, FUPSOL, and reconstructions following the four volcanic eruptions of 1808/9, 1815, 1831, and 1835. Left: Years 1 and 2 relative to 1780-1808, right: Years 3 to 7 relative to years 1 and 2. Hatching indicates where less than 8 out of 10 members (less 3 out of 4 for FUPSOL) agree in sign.

The heat uptake during the recovery phase does not occur in a globally uniform way. Composites for the FUPSOL and HadCM3 simulations for the four modelled early 19th century eruptions (Fig. 5) suggest that the equatorial Pacific cooled slightly less than the remaining oceans in the first two years after the eruptions, consistent with other studies.[35] In the subsequent five years, the central equatorial Pacific cooled further while the globe warmed. Although there is large within-ensemble variability (hatching) at these locations, the general pattern is consistent with the sea-surface temperature reconstruction that was used to force the palaeo-reanalysis.[36,13] Note that this reconstruction was designed to study decadal-to-multidecadal variability, while shorter-term variability is underestimated[37]. This might explain the rather weak signal.

The latter pattern is similar, though not identical, to the Pacific-Decadal Oscillation (PDO). a dominant climate mode. This suggests that the recovery from volcanic eruptions may resemble internal oceanic variability modes. This makes separation of forced and unforced climate variability difficult.

Growing glaciers

Other slow parts of the climate system might have reacted to the combined effect of five eruptions, too. Glacier length integrates and delays the primary climatic signal, and thus the volcanic forcing might have contributed to glacier growth. We analysed the length of four well-observed Alpine glaciers (Fig. 1b, note the inverted y-axis).[38-40] Concurrent with the drop in warm season temperature in the early 19th century, three of the four glaciers reached their maximum length around 1820. This is consistent with reduced melting due to volcanic summer cooling. All glaciers showed a second maximum in the 1850s (which for one glacier was longer than the first). By that time, Alpine temperature already increased (Fig. 1b).

204 However, based on bandpass-filtered sub-daily pressure measurements along a North-South
205 transect in Europe (see Methods) we find an intensification and southward shift of cyclonic
206 activity (predominantly in summer and autumn), which we interpret as an intensification and
207 a southward shift of the Atlantic-European cyclone track during the late 1830s, 1840s and into
208 the 1850s (Fig. S1). This is also mirrored in increased precipitation[41,42] and in multidecadal
209 changes in daily Alpine weather types derived from observations. Flood-prone, cyclonic types
210 during the warm season were more frequent from the mid-1810s until around 1880 than
211 before or after this period.[42] The second glacier advance is thus consistent with observed
212 climatic changes, but was arguably not a pure temperature effect.

213

214 **Southward shift of circulation**

215 A southward shift of the Atlantic-European cyclone track after volcanic eruptions was found
216 in a previous study and related to a weak African monsoon and consequent weakening of the
217 Atlantic-European Hadley cell.[43] After the last of the five early 19th century eruptions the
218 weak monsoons and southward shifted circulation persisted for ten years (Figs. 3, S1). A
219 southward shift of the northern subtropical jet and of the downwelling branch of the northern
220 Hadley cell in the 1830s to 1850s is also found in a zonal average in the palaeo-reanalysis
221 during the boreal warm season (Fig. S2). Furthermore, a recent reconstruction of the northern
222 tropical belt boundary based on tree-ring width also displays a southward shift in the first half
223 of the 19th century.[44] Hence, daily pressure observations, the palaeo-reanalysis and a tree-ring-
224 based reconstruction agree with each other and suggest a southward shift of circulation.

225 A possible cause for this is a negative phase of the Atlantic Multidecadal Oscillation (AMO)
226 in the 1830s to 1850s according to reconstructions.[36,45] This might have contributed to weak
227 African[46] and Indian monsoons[47] and to the southward shift of the northern tropical belt.[48] To

what extent the change in the AMO itself was related to the atmospheric circulation changes triggered by the eruptions, as was suggested for later eruptions,[49] or to decreased solar activity during the Dalton minimum,[50,51] or whether the AMO change was entirely unrelated to these forcings remains to be clarified.

Our analysis shows that the last phase of the LIA was characterised by large decadal-to-multidecadal climatic fluctuations.[21] In particular, a sequence of five volcanic eruptions within 28 years caused widespread global cooling, drying in central Africa, and a weakening of global monsoons, among other effects. The cooling in Europe favoured the growth of Alpine glaciers. The global temperature increase starting in the late 1830s therefore primarily reflects the recovery of the global climate system from a sequence of eruptions, with possibly a minor contribution from anthropogenic greenhouse gases.[7] From the late 19th and early 20th century onward, the greenhouse gas increase dominated the long term trend.[11,52] Additional, pronounced internal climate variability then catapulted global climate out of the LIA and into a first warm phase, the early 20th century warming.[42,53]

Methods

Palaeo-reanalysis

The palaeo-reanalysis EKF400 combines observations and proxies with an ensemble of 30 climate model simulations. The model used reconstructed sea-surface temperatures as boundary conditions as well as external forcings such as greenhouse gases and volcanic aerosols. The observations were assimilated using an off-line Ensemble Kalman Filter approach.[13]

Early instrumental observations

We used all series from GHCN-monthly (v3, adjusted)[14] with sufficient data (75% of the years must have data) in the reference period (1779-1808). To form a warm season average, 75% of months must have data. To form an average of all stations, 75% of stations must have data. The following stations were used: Kremsmünster, Wien, Prag, Paris, Karlsruhe, Berlin (2 series), München, Hohenpeissenberg, Budapest, Milano, Torino, Vilnius, De Bilt, Trondheim, Warsaw, St. Petersburg, Stockholm, Basel, Genf, Edinburgh, Greenwich, and New Haven.

Model simulations

FUPSOL: The ensemble simulations are based on the coupled atmosphere–chemistry–ocean model SOCOL-MPIOM (SOlar Climate Ozone Links coupled to the Max-Planck-Institute Ocean Model)[17]. It is run in a horizontal resolution of approximately 3.5 degrees with 39 levels up to 0.01 hPa. The four ensemble simulations from 1600-2000 are branched from control simulation for perpetual 1600 conditions and the volcanic forcing set to zero. The control simulation still shows some drift of roughly 0.05 K per 100 yrs and can be used to correct variables. The four transient simulations are forced by greenhouse gas concentrations, volcanic aerosol and solar spectral irradiance, the former similar to PMIP3 protocol[54] whereas the solar forcing is from Shapiro et al.[55], using the best estimate and the upper bound of the uncertainty. This results in a total solar irradiance change from the Maunder Minimum (1645-1715) to today of 6 W/m^2 (best estimate) and 3 W/m^2 (upper bound). Two ensemble members for each of the solar forcing setting are performed, respectively. A detailed description of the model and the simulations is given in Muthers et al.[17].

HadCM3: 10 ensemble members have been run using the coupled atmosphere–ocean model HadCM3.[56,57] The atmosphere has a horizontal resolution of 3.75 × 2.5 degrees in longitude and latitude with 19 levels. The ocean model has a resolution of 1.25 × 1.25 degrees with 20 levels. The ensemble members have been started in 1780 from the 4 all forced and the 4 NoAER ensemble members described in Schurer et al.[11] The simulations have very little drift and have initial conditions which account for all known forcings starting in 800AD[11]. The models are forced by PMIP3/CMIP5 protocol volcanic, solar, orbital, and anthropogenic forcings as described in Schurer et al.[11] The solar forcing used follows the Steinhilber et al.[58] dataset, spliced into the Wang et al.[59] dataset in 1810 and is therefore comparatively weaker than that used in the SOCOL-MPIOM model simulations. The volcanic forcing dataset used is Crowley and Unterman.[60] The only forcing which is different to that described in Schurer et al.[11] are the anthropogenic aerosols, which have been updated to follow the CMIP5

279 forcing following Smith et al.[61] Note that some simulations only start in 1780, hence 1780-1808 is used as
280 reference in HadCM3.

281

282 *Volcanic eruptions*

283 We considered five eruptions in Dec. 1808[8] (unknown), Apr. 1815 (Tambora), Oct. 1822 (Galanggung; note
284 that this eruption was not part of the model forcing, including the model underlying the reanalysis), Sep. 1831
285 (despite recent evidence of a possible misinterpretation of the 1831 Babuyan Claro eruption,[9] we kept an
286 eruption in that year due to enhanced sulphur in ice cores), and Jan. 1835 (Cosiguina), respectively. Post-
287 eruption warm seasons are those that start within 30 months of the eruption, i.e., 1809-11, 1815-17, 1823-25,
288 1832-33 and 1835-37 (for the Dec.-Feb. season in Fig. 3c the years are 1810-11, 1816-17, 1823-25, 1832-34,
289 1867-37).

290 For compositing the volcanic response in FUPSOL, where only annual mean values are analysed, we considered
291 all events in which the top-of-atmosphere net radiation exceeded -2 W m^{-2} relative to our reference period 1779-
292 1808 (this was considered as year 1). Twelve eruptions were selected in this way: 1600, 1641, 1673, 1693, 1719,
293 1761, 1809, 1815, 1831, 1835, 1884, 1991. We then referenced all segments to year 0 (the pre-eruption year;
294 which in no case rises above the background) and plotted years 0-10 (ending each segment when a new eruption
295 started). Significance was calculated by Monte Carlo sampling of segments over the 400 simulation years in the
296 non-eruption parts of the time series, assuming the same eruption probability ($p = 0.03$ yr^{-1}) as in the sample.
297 This procedure was then repeated 100 times to obtain 95% confidence intervals. No confidence interval was
298 calculated for Fig. 4d as the recovery ocean heat content is so slow that no non-eruption parts can be defined.

299

300 *Multi proxy reconstructions of Alpine temperature*

301 Trachsel et al.[15] related six tree-ring chronologies from the Alpine area to the summer temperature from the
302 HISTALP temperature dataset[20] composed of early instrumental and instrumental temperature measurements
303 spanning the period 1760-2008. The reconstruction[15] is based on partial least squares regression (PLS)[62]. PLS is
304 a regression technique based on a combination of dimension reduction and ordinary least squares regression
305 (OLS). In PLS the dataset is divided into dependent and independent variables. In the dimension reduction step,
306 a linear combination of dependent and independent variables is sought so that the correlation (or covariance)

between the two linear combinations is maximised. The linear combination of the dependent variables is then related to the linear combination of the independent variables using OLS regression. In our reconstruction[15] there is only one dependent variable to which the linear combination of the independent variables is related using OLS regression.

Trachsel et al.[15] split the tree-ring and instrumental data into high and low-frequency components. The low-frequency component was obtained using 31-year low-pass filtered data (using a Gaussian filter) and the high-frequency component is the residual of the 31-year low-pass filter (see Trachsel et al.[15] for detailed description of the method).

For the high frequency component, a normal OLS was used to relate PLS scores (linear combination of the proxy data) to the instrumental data. A univariate linear regression is defined as:

$$y = \alpha + \beta x + e \quad (1)$$

$$e \sim N(0, \sigma^2) \quad (2)$$

Where x are the PLS scores (linear combination of independent data), y is the measured temperature data, e are the residuals and σ^2 is the variance of the residuals. Model parameters were estimated in a Bayesian framework with uniform priors: $a \sim U(-\infty,\infty)$; $b \sim U(-\infty,\infty)$; $s \sim U(0,\infty)$

We then obtained predictions sampling from the posterior predictive distributions[63]. In contrast to the high frequency component, the low-pass filtered dataset is temporally autocorrelated. Therefore, normal OLS is not an appropriate method to relate PLS scores to instrumental data. Instead we used a model with an autoregressive term of order 1 (AR1) and autocorrelated residuals:

$$y(t) = \alpha + \beta x(t) + ar1\, y(t-1) + \varphi\, e(t-1) \quad (3)$$

Where x are the PLS scores (linear combination of independent data), y is the measured temperature data, e is the residual and indexes t and $t-1$ are the value of a time series at time steps t and $t-1$; β is the parameter relating the PLS scores to y, $ar1$ is the parameter relating the value of y at time step $t-1$ to the value of y at time step t and φ is the parameter relating the residual at time step $t-1$ to the residual at time step t. This model was run in a Bayesian framework using uniform priors for all parameters. To give some weight to the PLS scores, the prior of $ar1$ was:

$$ar1 \sim U(-0.65,0.65) \quad (4)$$

Both regression models ((1) and (3)) were run in a Bayesian framework, with three chains of 11000 iterations with 1000 iterations for adaptation (burn in) and a thinning interval of 10. This resulted in 3000 climate histories of low and high frequency, respectively. Combining all these histories resulted in an exceedingly large sample size of 9 million histories. Therefore, 100 histories of each component were chosen and all their possible 10000 combinations (i.e. sums) were assessed.

These 10000 internally consistent reconstructions were then smoothed with a 30-year running mean filter, resulting in an ensemble of smoothed reconstructions. The 2.5% and the 97.5% quantiles of these 30-year smoothed reconstructions were then used as confidence bounds for the 30-year smoothed reconstruction.

Cyclone track

To study the strength and position of the cyclone track over Europe we analysed daily or subdaily pressure data from 13 stations[64,65]: Amsterdam (4.9° E, 52.37° N), Armagh (6.64° W, 54.35° N), Basel (7.59° E, 47.56° N), Bern (7.45° E, 46.95° N), Geneva (6.14° E, 46.2° N), Gr. St. Bernard (7.19° E, 45.89° N), London (0.12° W, 51.51° N), Milan (9.19° E, 45.46° N), Paris (2.35° E, 48.86° N), Stockholm (18.06° E, 59.33° N), Torino (7.74° E, 45.12° N), Uppsala (17.63° E, 59.86° N), Zurich (8.54° E, 47.38° N). We used a 2-6 day bandpass Lanczos filter[66] with a 31 day convolution vector (as in Brugnara et al.[64]). Results were then expressed as anomalies from a 1961-1990 climatology from the closest grid point in the Twentieth Century Reanalysis 20CRv2c.[67]

Circulation indices

We analysed two zonal mean circulation indices from the palaeo-reanalysis. The positions of the northern subtropical jet and of the downwelling branch of the northern Hadley were determined as the position of the maximum zonal average zonal wind at 200 hPa and the position of the maximum zonal mean omega at 500 hPa, respectively, as described in in Brönnimann et al.[48] (we used the same settings as described for the SOCOL model simulations).

References

1. Zumbühl, H. J., Steiner, D. & Nussbaumer, S. U. 19th century glacier representations and fluctuations in the central and western European Alps: An interdisciplinary approach. *Glob. Plan. Change* **60,** 42-57 (2008).

2. Leclercq, P. W. et al. A data set of worldwide glacier length fluctuations. *The Cryosphere* **8,** 659–672 (2014).

3. Miller, G.H. et al. Abrupt onset of the Little Ice Age triggered by volcanism and sustained by sea-ice/ocean feedbacks. *Geophys. Res. Lett.* **39,** L02708 (2012).

4. PAGES 2k Consortium. Continental-scale temperature variability during the last two millennia. *Nat. Geosci.* **6,** 339–346 (2013).

5. Masson-Delmotte, V. et al. Information from paleoclimate archives. In: Stocker, T. F. et al. (eds.) *Climate Change 2013: The Physical Science Basis. Contribution of Working Group I to the Fifth Assessment Report of the IPCC.* Cambridge: Cambridge University Press, 383–464 (2013).

6. Crowley, T. J., Obrochta, S. P. & Liu J. Recent global temperature 'plateau' in the context of a new proxy reconstruction. *Earth's Future* **2,** 281–294 (2014).

7. Abram, N. J. et al. Early onset of industrial-era warming across the oceans and continents. *Nature* **536,** 411–418 (2016).

8. Guevara-Murua, A., Williams, C. A., Hendy, E. J., Rust, A. C. & Cashman, K. V. Observations of a stratospheric aerosol veil from a tropical volcanic eruption in December 1808: is this the Unknown ~ 1809 eruption? *Clim. Past* **10,** 1707-1722 (2014).

9. Garrison, C. S, Kilburn, C. R. J & Edwards, S. J. The 1831 eruption of Babuyan Claro that never happened: has the source of the one of the largest volcanic climate forcing events of the nineteenth century been misattributed? *J. Appl. Volcanol.* **7,** 8 (2018).

10. Schurer A., Tett S. F. B. & Hegerl G. C. Small influence of solar variability on climate over the last millennium. *Nat. Geosci.* **7,** 104-108 (2014).

11. Schurer, A., Hegerl, G.C., Mann, M., Tett, S. F. B. & Phipps, S. Separating forced from chaotic variability over the last millennium. *J Clim.* **26,** 6954–6973 (2013).

12. Raible C. C. et al. Tambora 1815 as a test case for high impact volcanic eruptions: Earth system effects. *WIRES Clim. Change* **7,** 569-589 (2016).

13. Franke, J., S. Brönnimann, J. Bhend & Y. Brugnara. A monthly global paleo-reanalysis of the atmosphere from 1600 to 2005 for studying past climatic variations. *Sci. Data* **4,** 170076 (2017).

14. Lawrimore, J. H. et al. An overview of the Global Historical Climatology Network monthly mean temperature data set, version 3. *J. Geophys. Res.* **116,** D19121 (2011).

15. Trachsel, M. et al. Multi-archive summer temperature reconstruction for the European Alps. *Quat. Sci. Rev.* **46,** 66–79 (2012).

16. Nicholson, S. E., Dezfuli, A. K. & Klotter, D. A two-century precipitation dataset for the continent of Africa. *B. Amer. Meteorol. Soc.* **93,** 1219–1231 (2012).

17. Muthers, S. et al. The coupled atmosphere–chemistry–ocean model SOCOL-MPIOM. *Geosci. Model Dev.* **7,** 2157-2179 (2014).

18. Sigl, M. et al. 19th century glacier retreat in the Alps preceded the emergence of industrial black carbon deposition on high-alpine glaciers. *The Cryosphere* **12,** 3311-3331 (2018).

19. Lüthi, M. P. Little Ice Age climate reconstruction from ensemble reanalysis of Alpine glacier fluctuations. *The Cryosphere* **8,** 639–650 (2014).

20. Böhm, R. et al. The early instrumental warm bias: a solution for long central European temperatures series 1760-2007. *Clim. Change* **101,** 41–67 (2010).

21. Neukom, R. et al. (2019). Consistent multi-decadal variability in global temperature reconstructions and simulations over the Common Era *Nat. Geosci.* (revised).

22. Hawkins, E. et al. Estimating Changes in Global Temperature since the Preindustrial Period. *Bull. Amer. Meteor. Soc,* **98,** 1841–1856 (2017).

23. Schurer, A. P., Mann, M. E., Hawkins, E., Tett, S. F. & Hegerl, G. C. Importance of the pre-industrial baseline for likelihood of exceeding Paris goals. *Nat. Clim. Change 7***,** 563-567 (2017).

24. Iles, C. & Hegerl, G. C. The global precipitation response to volcanic eruptions in the CMIP5 models. *Env. Res. Lett.* **9,** 104012 (2014).

25. Sontakke, N. A., Singh, N. & Singh, H. N. Instrumental period rainfall series of the Indian region (AD 1813–2005): Revised reconstruction, update and analysis. *The Holocene* **18,** 1055–1066 (2008).

26. Gallego, D., García-Herrera, R., Peña-Ortiz, C. & Ribera, P. The steady enhancement of the Australian Summer Monsoon in the last 200 years. *Sci. Rep.* **7,** 16166 (2017).

27 Hasselmann, K. Stochastic climate models part I. Theory. *Tellus,* **28,** 473-485 (1976).

28. Yu, Y. et al. Observed positive vegetation-rainfall feedbacks in the Sahel dominated by a moisture recycling mechanism. *Nat. Commun.* **8,** 1873 (2017).

29. Held, I. M. et al. Probing the Fast and Slow Components of Global Warming by Returning Abruptly to Preindustrial Forcing. *J. Clim.* **23,** 2418–2427 (2010).

30. Gupta, M. & Marshall, J. The Climate Response to Multiple Volcanic Eruptions Mediated by Ocean Heat Uptake: Damping Processes and Accumulation Potential. *J. Clim.* **31,** 8669–8687 (2018).
31. Ding, Y. et al. Ocean response to volcanic eruptions in Coupled Model Intercomparison Project 5 simulations. *J. Geophys. Res. Oceans* **119,** 5622–5637 (2014).
32. Stenchikov, G., Delworth, T. L., Ramaswamy, V., Stouffer, R. J., Wittenberg, A. & Zeng, F. Volcanic signals in oceans. *J. Geophys. Res.* **114,** D16104 (2009).
33. Gregory, J. M. et al. Climate models without preindustrial volcanic forcing underestimate historical ocean thermal expansion. *Geophys. Res. Lett.* **40,** 1600–1604 (2013).
34. Church, J.A. et al. Sea Level Change. In: In: Stocker, T. F. et al. (eds.) *Climate Change 2013: The Physical Science Basis. Contribution of Working Group I to the Fifth Assessment Report of the IPCC.* Cambridge: Cambridge University Press, 1137-1216 (2013).
35. Maher, N., McGregor, S., England, M. H. & Sen Gupta, A. Effects of volcanism on tropical variability. *Geophys. Res. Lett.* **42,** 6024–6033 (2015).
36. Mann, M. E. *et al.* Global signatures and dynamical origins of the Little Ice Age and Medieval Climate Anomaly. *Science* **326,** 1256-1260 (2009).
37. Franke, J., Frank, D., Raible, C. C., Esper, J. & Brönnimann, S. Spectral biases in tree-ring climate proxies, *Nat. Clim. Change* **3,** 360-364 (2013).
38. Zumbühl, H. J., Nussbaumer, S. U., Holzhauser, H. & Wolf, R. (Eds.) *Die Grindelwaldgletscher – Kunst und Wissenschaft.* Haupt, Bern, 256 pp (2016).
39. Nussbaumer, S. U., Zumbühl, H. J. & Steiner, D. Fluctuations of the Mer de Glace (Mont Blanc area, France) AD 1500–2050. Part I: The history of the Mer de Glace AD 1570–2003 according to pictorial and written documents. *Z. Gletscherk. Glazialgeol.* **40,** 5–140 (2007).
40. Nussbaumer, S. U. & Zumbühl, H. J. The Little Ice Age history of the Glacier des Bossons (Mont Blanc massif, France): a new high-resolution glacier length curve based on historical documents. *Clim. Change* **111,** 301-334 (2012).
41. Küttel, M., Luterbacher, J. & Wanner, H. Multidecadal changes in winter circulation-climate relationship in Europe: frequency variations, within-type modifications, and long-term trends. *Clim. Dyn.* **36,** 957-972 (2011).
42. Brönnimann, S. et al. Causes for increased flood frequency in central Europe in the 19th century. *Clim. Past Disc.,* cp-2019-17 (2019).

449 43. Wegmann, M. et al. Volcanic influence on European summer precipitation through monsoons: Possible
450 cause for "Years Without a Summer". *J. Clim.* **27,** 3683–3691 (2014).
451 44. Alfaro-Sánchez, R. et al. Climatic and volcanic forcing of tropical belt northern boundary over the past 800
452 years. *Nat. Geosci.* **11,** 933–938 (2018).
453 45. Gray, S. T., Graumlich, L. J., Betancourt, J. L. & Pederson, G. T. A tree-ring based reconstruction of the
454 Atlantic Multidecadal Oscillation since 1567 A.D. *Geophys. Res. Lett.,* **31,** L12205 (2004).
455 46. Martin, E. R. & Thorncroft, C. D. The impact of the AMO on the West African monsoon annual cycle. *Q. J.*
456 *R. Meteorol. Soc.,* **140,** 31–46 (2014).
457 47. Krishnamurthy, L. & Krishnamurthy, V. Teleconnections of Indian monsoon rainfall with AMO and Atlantic
458 tripole. *Clim. Dyn.,* **46,** 2269–2285 (2016).
459 48. Brönnimann, S. et al. Southward shift of the Northern tropical belt from 1945 to 1980. *Nat. Geosci.* **8,** 969-
460 974 (2015).
461 49. Birkel, S. D., Mayewski, P. A., Maasch, K. A., Kurbatov, A. V. & Lyon, B. Evidence for a volcanic
462 underpinning of the Atlantic multidecadal oscillation. *npj Climate and Atmospheric Science* **1,** 24 (2018).
463 50 Anet, J. G. et al. Impact of solar versus volcanic activity variations on tropospheric temperatures and
464 precipitation during the Dalton Minimum. *Clim. Past* **10,** 921-938 (2014).
465 51. Malik, A., Brönnimann, S. & Perona, P. Statistical link between external climate forcings and modes of
466 ocean variability. *Clim. Dyn.* **50,** 3649–3670 (2018).
467 52. Hegerl, G. C., Brönnimann, S., Schurer, A. & Cowan, T. The early 20th century warming: Anomalies,
468 causes, and consequences. *WIREs Clim. Change,* **9,** e522 (2018).
469 53. Brönnimann, S. Early twentieth-century warming. *Nat. Geosci.* **2,** 735-736 (2009).
470

471 **References in Methods Section**

472 54. Braconnot, P. et al. Evaluation of climate models using palaeoclimatic data. *Nat. Clim. Change*. **2,** 417-424
473 (2012).
474 55. Shapiro, A. I., Schmutz, W., Rozanov, E., Schoell, M., Haberreiter, M., Shapiro, A. V. & Nyeki, S. A new
475 approach to long-term reconstruction of the solar irradiance leads to large historical solar forcing. *Astronomy*
476 *and Astrophysics* **529,** A67 (2011).
477 56. Pope, V. D. et al. The impact of new physical parametrizations in the Hadley Centre climate model:
478 HadAM3. *Clim. Dyn.* **16,** 123– 146 (2000).

57. Gordon, C. et al. The simulation of SST, sea ice extents and ocean heat transports in a version of the Hadley Centre coupled model without flux adjustments. *Clim. Dyn.* **16,** 147– 168, (2000).

58. Steinhilber, F., Beer, J. & Fröhlich, C. Total solar irradiance during the Holocene. *Geophys. Res. Lett.* **36,** L19704 (2009).

59. Wang, Y-M., Lean, J. L. & Sheeley, N. R. Modeling the Sun's magnetic field and irradiance since 1713. *Astrophys. J.* **625,** 522–538 (2005).

60. Crowley, T. J. & Unterman, M. B. Technical details concerning development of a 1200-yr proxy index for global volcanism. *Earth Syst. Sci. Data* **5,** 187-197 (2013).

61. Smith, D. M. et al. Improved surface temperature prediction for the coming decade from a global climate model. *Science* **317,** 796-799 (2007).

62. Martens, H. & Naes, T. *Multivariate Calibration.* Wiley, Chichester, 423 pp. (1989).

63. Kruschke, J. *Doing Bayesian Data Analysis. A Tutorial with R, JAGS, and Stan.* Academic Press, London, 759 pp. (2014).

64. Brugnara, Y. et al. A collection of sub-daily pressure and temperature observations for the early instrumental period with a focus on the "year without a summer" 1816. *Clim. Past* **11,** 1027-1047 (2015).

65. Cram, T. A. et al. The International Surface Pressure Databank version 2. *Geosc. Data J.* **2,** 31-46 (2015).

66. Duchon, C. E. Lanczos filtering in one and two dimensions. *J. Appl. Meteorol.* **18,** 1016–1022 (1979).

67. Compo, G. P. et al. The Twentieth Century Reanalysis Project. *Q. J. R. Meteorol. Soc.* **137,** 1-28 (2011).

Corresponding author: Correspondence and requests for materials should be addressed to Stefan Brönnimann, email: stefan.broennimann@giub.unibe.ch

Acknowledgements. The work was supported by the Swiss National Science Foundation (projects 162668 and CRSII2-147659 and a personal grant to MT), by MeteoSwiss (CH2018) and by H2020 (ERC Grant PALAEO-RA, 787574).. Simulations were conducted at the Swiss Supercomputer Centre CSCS. GCH and AS were supported by the ERC-funded project TITAN (EC-320691) and by NERC under the Belmont forum, grant PacMedy (NE/P006752/1).

Author contributions. SB designed the study and performed most of the analyses. JFR performed the reanalysis. CCR performed the FUPSOL model simulations, AS performed the HadCM3 model simulations. CCR, AM, MW, AS, and MT processed the model simulations. JFR and JFL performed some of the analyses, SUN, DS, and HJZ analysed the glacier data. GCH assisted the analysis and interpretation of model data. All authors engaged in the discussion of results and contributed to writing the paper.

The authors declare no competing financial interests.

Data availability. The palaeo-reanalysis is available from http://cera-www.dkrz.de/WDCC/ui/Compact.jsp?acronym=EKF400_v1.1, instrumental temperature data from https://www.ncdc.noaa.gov/ghcnm/v3.php. The dryness indices for Africa are available from https://www1.ncdc.noaa.gov/pub/data/paleo/historical/africa/africa2001precip.txt, the Australian monsoon data from https://www.upo.es/vareclim/Data/Data_Index.php. The pressure data used are available from ISPD: https://reanalyses.org/observations/international-surface-pressure-databank. FUPSOL and HadCM3 model output can be donwloaded from https://boris.unibe.ch/id/eprint/130784.

Code availability. Code for the calculation of subtropical jet latitude and northern topical edge is from https://boris.unibe.ch/71204/. Code and input data for the reconstruction of Alpine summer temperature can be downloaded from https://boris.unibe.ch/id/eprint/130784.